Competing effects of proppant and surface roughness on the frictional stability of propped fractures

Jin Luo[1], Qi Zhang[1], Derek Elsworth[2], and Qi Zhao[3*]

[1]Faculty of Engineering, China University of Geosciences (Wuhan), Wuhan 430074, PR China

[2]Energy and Mineral Engineering and Energy Institute, The Pennsylvania State University, USA

[3]Department of Civil and Environmental Engineering, The Hong Kong Polytechnic University, Hung Hom, Hong Kong SAR, China

*Corresponding author: Qi Zhao (qi.qz.zhao@polyu.edu.hk)

Highlights

- Frictional behavior systematically transitions from fracture-dominated to proppant-dominated response as proppant mass loading increases.
- Proppants promote ductile shear failure that is exacerbated by increased proppant mass loading and increased grain size.
- The transition of frictional behavior caused by proppant could impact permeability and stability of the stimulated fractures.

Abstract

Proppant is often used to enhance reservoir stimulations such as hydraulic fracturing and hydraulic shearing, however, the influence of proppant on the shear deformation of fractures and the potential consequent induced earthquakes is rarely explored. We explore the systematics of frictional behavior, deformability and dilatancy of proppant-filled fractures to define the complex response to different fracture roughnesses and proppant mass loadings. Shear experiments on rough granite fractures show that proppant reduces cohesion and internal friction, reduces the shear stiffness, delays the shear displacement to a diminished peak strength, reduces the magnitude of shear dilation, and promotes ductile shear failure that is analogous to aseismic creep. A systematic transition in shear behavior occurs from fracture-roughness-dominant to proppant-dominant with increased proppant mass loading that is augmented by increased grain size. Long-wavelength fracture undulations may engage at large shear displacements, causing increased frictional resistance – identifying an intrinsic scale effect. The presence of proppant reduces the shear dilation. Thus, the convolved interactions between proppant and fracture roughness require careful assessment in their impact on creating and sustaining permeability and modes of aseismic versus seismic ruptures.

Keywords

Shear behavior, Proppant, Surface roughness, Frictional stability

1. Introduction

Reservoir stimulation methods such as hydraulic fracturing and hydraulic shearing are used to improve the efficiency of resource extraction from fractured hydrocarbon and geothermal reservoirs (e.g., Ahamed et al., 2021; Dempsey et al., 2015; KC & Ghazanfari, 2021; Rinaldi & Rutqvist, 2019; Schoenball et al., 2020; Zimmermann & Reinicke, 2010). Hydraulic fracturing involves the injection of fluid into a reservoir at a pressure higher than the minimum principal stress to create new hydraulic fractures that increase permeability. Conversely, hydraulic shearing reactivates shear deformation on pre-existing fractures by reducing the effective normal stress through fluid injection, promotes shear dilation (i.e., self-propping) that enhances permeability, but at a fluid pressure less than the minimum principal stress. Proppants are often injected with the fluid to maintain fracture permeability after injection. These stimulation processes modify the stress conditions on rock discontinuities, may generate shear deformation that could induce earthquakes (Guglielmi et al., 2015) with the presence of proppant making the stress state in fractured rock mass more difficult to predict.

Commonly used proppant types include silica sands, ceramic particles and resin-coated sands, among other high-strength natural and artificial granular materials. The sizes of such proppants are generally between 8 and 140 mesh (105 μm – 2.38 mm) (Liang et al., 2016). Silica sand is the most commonly used proppant for reservoir stimulation because of its low cost and adequate performance, while engineered proppants may offer better stimulation results but at higher costs. Much interest has been applied to the permeability enhancement resulting from proppant treatment. The evolution of permeability of a propped fracture using shearing-concurrent measurements of permeability at constant velocity shearing shows permeability of a propped fracture to be mainly governed by the normal stress, the proppant thickness, and the proppant size

(Zhang et al., 2017). However, few studies have focused on the frictional stability of propped fractures, in particular where the proppant loading is low relative to the roughness of the native fracture – and hence the competition between the proppant pack and native fracture will be important. Proppant embedment during rock shearing under different rock roughness conditions indicates that proppant caused a reduction of the rock fracture mechanical properties including peak shear strength, shear stiffness and friction angle, and enhances surface damage (Tang & Ranjith, 2018; Tang et al., 2019). Cornelio and Violay (2020) performed a parametric analysis that described the Sommerfeld number, which is a key parameter assessing the effectiveness of elastohydrodynamic lubrication during seismic sliding and observed that the injection of proppant can allow the fault to slip into the fully elastohydrodynamic lubrication regime with a small friction coefficient.

Conversely, studies on the shear behavior of filled rock discontinuities in geophysics and rock mechanics also provide valuable insights. Early studies suggested that filled rock discontinuities exhibit lower strengths and effective frictional coefficients than unfilled discontinuities (Barton, 1974). Later studies on the shear behavior of filled rock discontinuities identified similar effects for different rock types, filling materials and stress conditions. de Toledo and de Freitas (1993) reviewed studies related to the shear strength of infilled rock joints in the literature, discussed the main parameters controlling the shear strength of infilled joints and provided a framework for understanding the failure mechanisms involved in the shearing of such discontinuities. They concluded that the shear mechanisms were controlled by the grain size, the thickness of filler material and the rock itself. Indraratna et al. (2010) presented possible shearing mechanisms that may occur in soil-infilled rock joints and proposed a corresponding joint shear strength criterion that considers the effects of a series of governing parameters such as the friction

angle of the infill material, the basic friction angle of the rock joint, the degradation of asperities and the infill thickness to asperity height ratio. Jahanian and Sadaghiani (2014) performed a series of constant normal load direct shear tests to investigate the shear strength of artificial samples with infilled rough joint surfaces having different asperity and infill characteristics. They found that the normal stress on the joint played an important role in the shear behavior of infilled rock joint samples. Meng et al. (2017) studied the shear behaviors of joints with thin layers of different infillings and found that the maximum shear strength of the filled joints was significantly reduced compared with the clean joints. Moreover, when the joint infill was of large granular particles, the particles rotated and were crushed. Tang et al. (2020) studied the shear behavior and mechanisms of clean and filled rough joints under direct shear tests using experimental and numerical approaches with the mechanisms of the shear stress and shear dilatancy behavior significantly altered by the infilling material. Zhao et al. (2020) performed direct shear experiments on sand and clay infilled joints prepared by reproducing the standard Joint Roughness Coefficient (JRC) profiles on a rock-like material and placing the infill material inside the joint. Their results showed that the shear behavior and strength of the infilled joints were affected by the JRC, the infill material type, the infill thickness to joint asperity amplitude ratio and the applied normal stress.

These observations are congruent to those of fault gouge where the gouge, itself, dominates the frictional response of mature faults. For example, Marone (1998); Marone et al. (1990) discussed shear localization in fault gouge. Their data highlight differences in the shear behavior of bare rock surfaces as compared to shear within granular fault gouge that can dilate and deform. An investigation of the frictional properties and stability of frictional sliding was presented, and the effect of surface roughness, gouge thickness, and slip rates was studied.

Surface roughness of the fractures is an important factor controlling the frictional stability of rock discontinuities across a large range of scales. Bandis et al. (1981) noted the significance of scale effects on both the shear strength and deformation characteristics with both the geometrical and strength characteristics of surface roughness presented as potential sources of scale effects. At large fault scale, Brodsky et al. (2016) quantified the slip surface roughness by measuring the aspect ratio and pointed out that faults have scale-dependent roughness. Surface roughness also influences proppant embedment under shear deformation and in turn influences the shear behavior of fractured rocks. Tang and Ranjith (2018) studied proppant embedment during rock shearing under different fluid and rock roughness conditions. They found that a rough surface achieves a higher embedment increment than smooth rock due to severe dilation. However, the influences of proppant relative to the roughness of the encasing fractures have yet to be systematically evaluated and their impact on shear strength and frictional stability determined.

Reservoir stimulation aided by proppant plays an important role in the efficient and safe extraction of hydrocarbon and geothermal energy from fractured reservoirs, which are critical to the energy transition towards carbon neutrality. Therefore, to resolve the ambiguous impact of proppant-fracture roughness interaction on the frictional stability of propped fractures, we systematically explore the frictional behavior of rough rock fractures under different proppant and normal stress conditions and use quantitative surface roughness analysis to elucidate the underlying mechanisms.

2. Material and Methods

Outcrop samples of granite were collected that are representative of the Gonghe geothermal site (Gonghe basin, Qinghai province, China). The granite mainly consists of quartz (20%–30%), plagioclase (25%–35%), alkaline feldspar (30%–38%) and mica (5%–7%), with a dry density of

2.62–2.65 g/cm^3. The rock samples were cut into 100 mm sized cubes and then split into two equal-sized halves using indirect tensile (knife-edge) loading. This created the matching rough fractures that we examined in this study (Figure 1).

Figure 1. Preparation process for the rough granite fractures used in the direct shear tests. (a & b) Indirect tensile fracture loading to create a fresh rough fracture with matching surfaces. (c) Silica sand proppant placement on the fracture surface using dry pluviation. (d) Test setup of the direct shear test.

Three quartz sand samples with monomodal grain size ranges (0.1–0.5 mm, 0.5–1.0 mm, and 1.0–2.0 mm) were used as proppant and sandwiched between the rough fracture surfaces. For each proppant sample, 2 g of the proppant was placed on the fracture surface by dry pluviation. Proppant placement in narrow and rough fractures under reservoir conditions is equivocal and likely patchy, as the proppant interacts with the flow of the injection fluid and the specifics of the local fracture roughness (Wang et al., 2018). Our method provides a pragmatic and repeatable procedure to create a heterogeneous proppant layer partially covering the fracture, which is preferred in practice because it drastically increases the fracture conductivity (Bolintineanu et al., 2017; Medina et al., 2018).

Before the direct shear tests, tilt tests were conducted on the rough fractures with four proppant conditions as well as on a planar, smooth and pristine fractures to measure the basic friction angle (ϕ_b) of the fractures under low stress. Then, three suites of direct shear experiments under constant normal stresses were conducted at a constant shear rate of 0.01 mm/s to a maximum shear displacement of 15 mm. The first suite comprised 16 shear experiments representing combinations of four normal stresses (σ_n = 2 MPa, 3 MPa, 4 MPa, and 5 MPa) and the four

proppant conditions (no proppant and three abovementioned proppant samples, referred to as P0.0, P0.1, P0.5, and P1.0, respectively). To ensure the reliability of the data, the second suite of 6 experiments was conducted under the conditions where anomalous frictional behavior was observed. The third suite of experiments examined the role of proppant mass loading (i.e., the amount of proppant by weight) – all at 4 MPa and with P0.1 proppant, but with different mass loadings of proppant at 4g, 6g, and 8g. During the direct shear experiments, shear stress (τ), shear displacement (δ_s) and dilation (δ_v) were simultaneously monitored at a sampling rate of 2.5 Hz. The apparent friction coefficient is calculated as $\mu = \tau/\sigma_n$. Note that we conducted constant normal stress direct shear tests, thus, the overall variations of the shear stress and the apparent friction coefficient are identical.

We used a surface scanner to digitize the two sides of the surfaces of each fracture, both pre- and post- experiments, at a spatial resolution of 30 μm. The comminuted gouge material on the specimens post-experiments was removed with a soft brush before scanning. Each surface scan generates a point cloud representing the fracture surface geometry, and we calculate the roughness amplitude (H) as the difference between the highest peak and lowest trough on the surface. We re-sampled the point cloud onto a 50 μm-sized regular mesh. Then, a total of nine equal-spaced profiles were extracted from the surface along the shear direction (Figure 2). We examined the roughness of the extracted profiles quantitatively using the RMS roughness (i.e., Root Mean Square of the profiles amplitude) and Z_2 (i.e., RMS of the second derivative of the profiles amplitude) (Magsipoc et al., 2019; Myers, 1962; Tse & Cruden, 1979). Then, the roughness parameters Z_2 and RMS of the profiles were averaged to obtain the mean roughness of the surface. Finally, the variation of surface roughness both pre- and post-tests (ΔZ_2 and ΔRMS) for both sides of the fractures was evaluated from the differences in these roughness parameters.

Figure 2. Fracture surface roughness measurement and calculations. (a) Surface scan setup. The surface was digitized into a point cloud with 30 μm spatial resolution. (b) Example results of the surface scan showing the morphological information pre- then post-test (post-test scan was conducted after removing the gouge). The averaged surface roughness was calculated based on nine profiles measured along the shear direction. (c) Example of actual surfaces pre- and then post-test, corresponding to (b).

Results

Figure 3. Tilt tests results on rough fractures with four proppant conditions (P0.0, P0.1, P0.5, and P1.0) as well as on a flat, smooth, and pristine fracture to measure the basic friction angle (ϕ_b).

Figure 4. Apparent friction coefficient (a-d) and dilation (e-h) as functions of shear displacement of the fractures under different normal stress and proppant conditions. Solid lines and dashed lines are from the first and second suites of repeated experiments, respectively. Inserts in (a) show the example proppant grains under the microscope. PX.X mnemonics indicate the grain size of the proppant in mm.

The averaged ϕ_b values from the tilt tests for proppant conditions P0.1, P0.5, and P1.0 were 46.13°, 40.03°, and 35.29°, respectively – all lower than the averaged ϕ_b of the non-propped specimens at 61.46° but higher than the averaged ϕ_b obtained on a flat saw cut surface with no proppant of 26° (Figure 3).

In the non-propped direct shear experiments, the apparent friction coefficient, μ, increased linearly with the shear displacement, δ_s, to a peak value, μ_p (i.e., static frictional strength) followed by an abrupt drop (Figure 4 a-d). Then, μ decreased to a residual value. In the propped direct shear experiments, μ also increased with δ_s; however, the rate of increase was decreased, that is, the

proppant reduced the shear stiffness of the fracture. When σ_n < 5 MPa, the reduction of shear stiffness increased with increasing proppant size. When σ_n = 5 MPa, the grain size of the proppant did not show a clear influence on the shear stiffness – the fractures had similar shear stiffness values regardless of the proppant grain size. Non-propped specimens had μ_p values close to 2, significantly higher than those of the propped specimens, with greater reductions resulting from larger sized proppants.

The peaks of the apparent friction coefficient-shear displacement (μ-δ_s) curves for the propped samples became less pronounced relative to residual μ (i.e., less brittle), and the larger the proppant grain size, the more significant was this effect. Several experiments with proppants P0.5 and P1.0 returned a flat peak response (with δ_s). Instead, the μ stabilized around the reduced μ_p. In addition, the occurrence of μ_p was delayed by the proppant; and the larger the proppant grain size, the larger the delay, except for the experiments conducted under 5 MPa, in which the delay showed no obvious correlation with proppant grain size.

In a typical direct shear experiment, the vertical displacement, δ_v, experienced a transition from compaction (negative δ_v) to dilation (positive δ_v) with increased shear displacement. The non-propped experiments lack the compaction phase with the propped experiments showing compression over an extended δ_s (Figure 4 e-h). Most observations followed this general trend, but the forms of the δ_v-δ_s dilation curves were altered. The larger the proppant grain size, the more significant was the compression phase, with correspondingly less dilation. Overall, experiments with low σ_n had higher dilation values than those under high σ_n. Also, in experiments with low σ_n, the dilation was generally still increasing at the end of the experiments after δ_s>15mm. Only propped experiments conducted at 5 MPa showed plateaus at the end of experiments, suggesting that ultimate dilation had been reached.

Table 1. Peak shear strengths recovered from the shear tests.

The shear strength of the first two suites of experiments can be described with linear failure envelopes (Figure 5a): $\tau_{\mathrm{p}} = s + \mu_{\mathrm{i}}\sigma_n$, where the intercept s is the cohesion and μ_{i} is the internal friction that describes the rate that shear strength (τ_{p}, see Table 1 for peak shear stress values) increases with σ_{n}. The s values for the four sets of experiments with different proppant conditions (P0.0, P0.1, P0.5, and P1.0) were 1.28 MPa, −0.84 MPa, −1.00 MPa, and −0.62 MPa; respectively; and the μ_{i} values were 1.40, 1.38, 1.29, and 1.09, respectively. With the introduction of the proppant, the internal friction and the cohesion were reduced, and the larger the proppant grain size, the more significant were the two effects. The flattened and lowered failure envelope, together with injection fluid pressure, would render the stimulated fractures in the field more susceptible to shear failure (Figure 5b). In addition, the dilation at μ_{p} ($\delta_{\mathrm{v,p}}$) showed no obvious correlation with normal stress or proppant conditions (Figure 5c); whereas, the dilation at 15 mm of shear displacement ($\delta_{\mathrm{v,15mm}}$) decreased with increasing proppant grain size (Figure 5d).

Figure 5. Summary of shear behavior for different normal stress and proppant conditions. (a) Peak shear stress (τ_{p}) as a function of normal stress (σ_{n}). (b) Schematic of failure envelope relative to effective principal stresses (σ_1' and σ_3'). (c) Dilation at peak shear stress. (d) Dilation at 15 mm of shear displacement. Dashed lines are linear regressions.

For the six experiments with apparently anomalous frictional behavior in the first suite of experiments, a significant increase of δ_{s} occurred with negligible variations of τ or δ_{v}. This shear behavior was repeated in most of the second suite of experiments; ruling out the extrinsic origin

of this behavior. Such sliding behavior with substantial shear displacement at relatively constant shear stress was analogous to aseismic creep observed in earthquake studies (Rathbun & Marone, 2010). This stable sliding behavior had no apparent correlation with proppant size and was absent in experiments under σ_n = 5 MPa.

Figure 6. Results of the direct shear experiments conducted under 4 MPa normal stress and with different mass loadings of P0.1 proppant. (a) Illustration of different mass loadings of proppant at 2, 4, 6 and 8 grams mass loading per fracture. (b & c) Shear stress and dilation curves.

The increased mass loading of proppant caused a larger area of proppant coverage on the fracture surface as well as an increased thickness of the proppant layer, especially in the troughs (Fig 5a). The third suite of experiments showed that the larger and thicker proppant caused the aseismic creep behavior. The more proppant, the longer the creep distance, the gentler the peak of the μ-δ_s curve, and the smaller the shear dilation (Fig 5 b&c).

Figure 7. Change in fracture surface roughness (ΔZ_2 and ΔRMS) from pre- to post- experiments and for different normal stress and proppant conditions.

The variation of surface roughness due to the shear deformation showed a clear correlation with proppant conditions (Figure 7, see Table 2 for detailed roughness values). The non-propped samples showed the largest variation in roughness with the samples propped by P0.1 and P0.5 proppants experienced only minor changes in roughness. The samples propped by P1.0 proppant showed a greater variation in roughness relative to the other two proppant size experiments, but less than the non-propped experiments.

275

276 **Table 2.** Surface roughness statistics measured both pre- and post-test (roughness amplitude (H)
277 is the difference between maximum height and minimum height, RMS is the Root Mean Square
278 roughness, and Z_2 is the RMS of the second derivative of the extracted profiles.

279

280 **Discussion**

281 The frictional behavior was significantly altered by proppant. Proppant reduced the shear
282 stiffness of the fractures, extended the shear displacement, δ_s, to the occurrence of peak friction,
283 μ_p, and diminished the peak response. In the non-propped experiments, the abrupt drop of μ
284 indicates brittle shear failure, which is related to the sudden release of strain energy associated to
285 asperity breakage. Shear failure of the propped fractures is ductile and lacks such a rapid energy
286 release process – the ductility increases with increased proppant grain size and mass loading.

287 The failure envelopes can be used to determine the proximity to failure, the value of *s*
288 represents the shear strength at no normal stress and is related to the interlocking of the asperities.
289 The non-propped fractures returned positive *s* values and the propped fractures negative *s* values.
290 This indicates that the proppant not only prevents the asperity from interlocking but also creates
291 an additional lubrication effect that makes the fracture mobile – analogous to acting as a ball-
292 bearing race. This conjecture is also supported by tilt tests, where we observed a systematic
293 decrease of the basic friction angle with the increase of proppant size (Figure 3). These adverse
294 influences on the frictional stability of propped fractures are more prominent when the proppant
295 grain size was relatively large and/or when the mass loading of the proppant was relatively high.

296 Both shear stiffness and peak response are related to the interlocking of asperities at the
297 initial stage of shearing. Propped fractures showed similar shear behavior to rock fractures under

cyclic, repeated, or continuous shear steps (e.g., Grasselli & Egger, 2003; Lee et al., 2001; Zhao et al., 2018). In such tests, the fracture surfaces are damaged, and the asperities worn. For our proppant-filled fractures, however, the surface roughness analysis showed that the fractures experienced insignificant damage. This suggests that proppant protected the asperities by preventing their interlocking and interactions. For the same proppant mass loading, this protective effect is more noticeable as proppant size decreases. The surface roughness of the tested specimen with proppant grain size >1 mm showed variations of roughness, especially at relatively high σ_n, suggesting surface damage. This may be because small proppant grains readily infill the troughs; while larger grains tend to engage with asperities that eventually cause damage. Moreover, high normal stress intensifies the asperity-asperity and asperity-fracture interactions.

In all the propped experiments, the thickness of the proppant layer was smaller than the roughness amplitude, which introduced an extra degree of complexity due to the interactions between proppant and fracture surfaces. This is manifest as the creep behavior that has not been investigated in previous studies. Previous studies considered fractures that are either clean or fully covered by granular layers, which may not be representative of actual proppant placement conditions. We found that partially filled fractures may not exhibit typical stress-strain curves, and thus, cannot be described with formerly established constitutive relations. The complex shear behavior of propped fractures can be explained by the interaction of proppant with roughness at different scales (Figure 8 a-e). Bare fractures experience asperity-asperity interlocking, causing significant shear resistance, dilation, and surface damage (Figure 8a). With a low mass loading of proppant, proppant grains buffer the small-scale asperities (i.e., unevenness) from direct contact, and the rolling of proppant grains may also contribute to the shear behavior (Pereira, 1997), thus, lowering the shear strength and preventing the damaging of asperities (Figure 8b). The creep

behavior appears as the proppant layer is sufficiently thick to fill the troughs on the rough surface, allowing the fracture to slide on proppant alone (Figure 8c). However, as the shear displacement increases, large-scale fracture undulation (i.e., waviness) allows the opposite fracture faces to engage and the creep behavior stops. The more proppant, the longer the creep displacement that can occur. The ultimate form of this creep behavior would occur when a thick proppant bed covers the entire fracture surface and obviates the influence of the long wavelength roughness by preventing the fracture asperities from engaging, even at maximum shear (Figure 8d). This will result in a much flatter μ-δ_s curve with much lower shear strength than for bare fractures. This phenomenon is evident from the numerous shear tests on fully filled fractures reported in the literature (e.g., de Toledo & de Freitas, 1993; Indraratna et al., 2010; Jahanian & Sadaghiani, 2014; Meng et al., 2017; Tang et al., 2020; Zhao et al., 2020). This transition in shear behavior from fracture response to proppant response is favored by increasing the mass loading of proppant and by increasing proppant grain size.

Figure 8. Schematic of mechanisms describing the transition of fracture shear behavior from control by fracture roughness (a) to control by proppant strength (d) with increasing mass loading of the proppant. (a-d) Mechanistic illustration of shear behavior with increasing proppant mass loading. (e) Representative τ-δ_s curves corresponding to (a-d).

Fluid injection during reservoir stimulation may promote aseismic creep on rock discontinuities that could ultimately translate to seismic rupture (Guglielmi et al., 2015; Zoback, 2012). Our study shows that proppant-filled fractures can also respond in this manner with ductile shear failure occurring through the asperity-shielding mechanism. The ductile shear failure, if generated in situ, will be invisible to seismic monitoring methods and absent from the seismic energy budget. This may be especially important for fractures only partially infilled by proppant

that are under shear deformation, for example, natural fractures obliquely intersecting the main driven hydraulic fracture and intentionally hydro-sheared fractures.

Shear dilation due to the surface roughness, i.e., self-propping, can keep fractures open even at high effective normal stress (Brace, 1980; Durham & Bonner, 1994). This is desired in reservoir stimulation but will be suppressed by the presence of proppant - where the shear dilation potential of the fracture will be ceded to that of the proppant. Even though proppant placement can increase the fracture aperture, our results demonstrated that the propped fracture also experiences less shear dilation, especially at large shear displacement. This effect needs to be considered for effective shear stimulations.

The results we obtained in this study are from fractures with different initial roughness values. The fact that we observe the transition of frictional behavior without controlling the surface roughness of the fracture specimens indicates that these are systematic first-order dependencies that override the impacts of the specific variabilities in fracture roughness. However, at higher stresses (>5 MPa), the presence of proppant does not significantly alter the shear behavior, relative to that at lower normal stresses. These observations suggest that there is an interplay among the influences of fracture surface roughness, proppant conditions, and normal stress. Understanding this relationship may be the key to optimally increasing permeability in stimulated reservoirs and in concurrently mitigating induced seismicity. Although our experiments are conducted under dry conditions and at relatively low effective stresses, the overall trends in proppant response will apply at the reservoir scale.

Conclusion

We systematically investigate the influence of proppant on the frictional behavior of rough granite fractures. Importantly, we observe that proppant plays an opposing role to surface roughness: thick proppant layers prevent asperities from interlocking and protect the surface from damage but render the fracture weaker in shear. We summarize the influences of proppant on shear behavior into four key observations: (i) reduction of the cohesion and internal friction; (ii) reduction of shear stiffness and extension of the shear displacement to reach the diminished peak strength; (iii) reduction of shear dilation; and (iv) promotion of ductile shear failure – all are exacerbated by increased mass loading and increased mean grain size of the proppant. Proppant placement and fracture shear dilation can both enhance the permeability of the stimulated fractures, but the presence of proppant reduces the dilation; thus, the interaction between proppant and fracture self-propping requires careful assessment. In addition, the ductile shear failure that is analogous to aseismic creep on propped fractures is likely at high proppant mass loadings. As proppants are widely used in hydrocarbon and some geothermal reservoir stimulations, it is important to understand the interplay of surface roughness, effective normal stress, and proppant conditions on rock discontinuities to ensure the efficiency of energy extraction and alleviation of hazardous induced seismicity.

Acknowledgments

Q. Zhao is supported by the Hong Kong Polytechnic University (Start-up Fund No. P0034042) and the Early Career Scheme of the Research Grants Council of the Hong Kong SAR, China (No. PolyU 25220021). J. Luo acknowledges the support of the National Natural Science Foundation of China (No. 41877200). D. Elsworth gratefully acknowledges support from the G. Albert Shoemaker endowment. Test data presented in this paper is available in https://doi.org/10.6084/m9.figshare.20078678.v1.

Statements and Declarations

The authors declare that there is no conflict of interest.

References

Ahamed, M. A. A., Perera, M. S. A., Elsworth, D., Ranjith, P. G., Matthai, S. K. M., & Dong-yin, L. (2021). Effective application of proppants during the hydraulic fracturing of coal seam gas reservoirs: Implications from laboratory testings of propped and unpropped coal fractures. *Fuel, 304*. https://doi.org/10.1016/j.fuel.2021.121394

Bandis, S., Lumsden, A. C., & Barton, N. R. (1981). Experimental studies of scale effects on the shear behaviour of rock joints. *International Journal of Rock Mechanics and Mining Sciences & Geomechanics Abstracts, 18*(1), 1-21. https://doi.org/10.1016/0148-9062(81)90262-x

Barton, N. (1974). A review of the shear strength of filled discontinuities in rock. *Norwegian Geotechnical Institute Publication, 105*.

Bolintineanu, D. S., Rao, R. R., Lechman, J. B., Romero, J. A., Jove-Colon, C. F., Quintana, E. C., Bauer, S. J., & Ingraham, M. D. (2017). Simulations of the effects of proppant placement on the conductivity and mechanical stability of hydraulic fractures. *International Journal of Rock Mechanics and Mining Sciences, 100*, 188-198. https://doi.org/10.1016/j.ijrmms.2017.10.014

Brace, W. F. (1980). Permeability of crystalline and argillaceous rocks. *International Journal of Rock Mechanics and Mining Sciences & Geomechanics Abstracts, 17*(5), 241-251. https://doi.org/10.1016/0148-9062(80)90807-4

Brodsky, E. E., Kirkpatrick, J. D., & Candela, T. (2016). Constraints from fault roughness on the scale-dependent strength of rocks. *Geology, 44*(1), 19-22. https://doi.org/10.1130/g37206.1

Cornelio, C., & Violay, M. (2020). Parametric analysis of the elastohydrodynamic lubrication efficiency on induced seismicity. *Geophysical Journal International, 222*(1), 517-525. https://doi.org/10.1093/gji/ggaa180

de Toledo, P. E., & de Freitas, M. H. (1993). Laboratory testing and parameters controlling the shear strength of filled rock joints. *Géotechnique, 43*(1), 1-19. https://doi.org/10.1680/geot.1993.43.1.1

Dempsey, D., Kelkar, S., Davatzes, N., Hickman, S., & Moos, D. (2015). Numerical modeling of injection, stress and permeability enhancement during shear stimulation at the Desert Peak Enhanced Geothermal System. *International Journal of Rock Mechanics and Mining Sciences, 78*, 190-206. https://doi.org/10.1016/j.ijrmms.2015.06.003

Durham, W. B., & Bonner, B. P. (1994). Self-propping and fluid flow in slightly offset joints at high effective pressures. *Journal of Geophysical Research: Solid Earth, 99*(B5), 9391-9399. https://doi.org/10.1029/94jb00242

Grasselli, G., & Egger, P. (2003). Constitutive law for the shear strength of rock joints based on three-dimensional surface parameters. *International Journal of Rock Mechanics and Mining Sciences, 40*(1), 25-40. https://doi.org/10.1016/s1365-1609(02)00101-6

Guglielmi, Y., Cappa, F., Avouac, J. P., Henry, P., & Elsworth, D. (2015, Jun 12). Seismicity triggered by fluid injection-induced aseismic slip. *Science, 348*(6240), 1224-1226. https://doi.org/10.1126/science.aab0476

Indraratna, B., Oliveira, D. A. F., & Brown, E. T. (2010). A shear-displacement criterion for soil-infilled rock discontinuities. *Géotechnique, 60*(8), 623-633. https://doi.org/10.1680/geot.8.P.094

Jahanian, H., & Sadaghiani, M. H. (2014). Experimental Study on the Shear Strength of Sandy Clay Infilled Regular Rough Rock Joints. *Rock Mechanics and Rock Engineering, 48*(3), 907-922. https://doi.org/10.1007/s00603-014-0643-4

KC, B., & Ghazanfari, E. (2021). Geothermal reservoir stimulation through hydro-shearing: an experimental study under conditions close to enhanced geothermal systems. *Geothermics, 96*. https://doi.org/10.1016/j.geothermics.2021.102200

Lee, H. S., Park, Y. J., Cho, T. F., & You, K. H. (2001). Influence of asperity degradation on the mechanical behavior of rough rock joints under cyclic shear loading. *International Journal of Rock Mechanics and Mining Sciences, 38*(7), 967-980. https://doi.org/10.1016/s1365-1609(01)00060-0

Liang, F., Sayed, M., Al-Muntasheri, G. A., Chang, F. F., & Li, L. (2016). A comprehensive review on proppant technologies. *Petroleum, 2*(1), 26-39. https://doi.org/10.1016/j.petlm.2015.11.001

Magsipoc, E., Zhao, Q., & Grasselli, G. (2019). 2D and 3D Roughness Characterization. *Rock Mechanics and Rock Engineering, 53*(3), 1495-1519. https://doi.org/10.1007/s00603-019-01977-4

Marone, C. (1998). Laboratory-Derived Friction Laws and Their Application to Seismic Faulting. *Annual Review of Earth and Planetary Sciences, 26*(1), 643-696. https://doi.org/10.1146/annurev.earth.26.1.643

Marone, C., Raleigh, C. B., & Scholz, C. H. (1990). Frictional behavior and constitutive modeling of simulated fault gouge. *Journal of Geophysical Research, 95*(B5). https://doi.org/10.1029/JB095iB05p07007

Medina, R., Detwiler, R. L., Prioul, R., Xu, W., & Elkhoury, J. E. (2018). Settling and Mobilization of Sand-Fiber Proppants in a Deformable Fracture. *Water Resources Research, 54*(12), 9964-9977. https://doi.org/10.1029/2018wr023355

Meng, F., Zhou, H., Wang, Z., Zhang, L., Kong, L., Li, S., & Zhang, C. (2017). Influences of Shear History and Infilling on the Mechanical Characteristics and Acoustic Emissions of Joints. *Rock Mechanics and Rock Engineering, 50*(8), 2039-2057. https://doi.org/10.1007/s00603-017-1207-1

Myers, N. O. (1962). Characterization of surface roughness. *Wear, 5*(3), 182-189. https://doi.org/10.1016/0043-1648(62)90002-9

Pereira, J. P. (1997). Rolling friction and shear behaviour of rock discontinuities filled with sand. *International Journal of Rock Mechanics and Mining Sciences, 34*(3-4), 244.e241-244.e217. https://doi.org/10.1016/s1365-1609(97)00037-3

Rathbun, A. P., & Marone, C. (2010). Effect of strain localization on frictional behavior of sheared granular materials. *Journal of Geophysical Research, 115*(B1). https://doi.org/10.1029/2009jb006466

Rinaldi, A. P., & Rutqvist, J. (2019). Joint opening or hydroshearing? Analyzing a fracture zone stimulation at Fenton Hill. *Geothermics, 77*, 83-98. https://doi.org/10.1016/j.geothermics.2018.08.006

Schoenball, M., Ajo-Franklin, J. B., Blankenship, D., Chai, C., Chakravarty, A., Dobson, P., Hopp, C., Kneafsey, T., Knox, H. A., Maceira, M., Robertson, M. C., Sprinkle, P., Strickland, C., Templeton, D., Schwering, P. C., Ulrich, C., & Wood, T. (2020). Creation of a Mixed-Mode

Fracture Network at Mesoscale Through Hydraulic Fracturing and Shear Stimulation. *Journal of Geophysical Research: Solid Earth, 125*(12). https://doi.org/10.1029/2020jb019807

Tang, J.-Z., Yang, S.-Q., Zhao, Y.-l., & Tian, W.-L. (2020). Experimental and numerical modeling of the shear behavior of filled rough joints. *Computers and Geotechnics, 121*. https://doi.org/10.1016/j.compgeo.2020.103479

Tang, Y., & Ranjith, P. G. (2018). An experimental and analytical study of the effects of shear displacement, fluid type, joint roughness, shear strength, friction angle and dilation angle on proppant embedment development in tight gas sandstone reservoirs. *International Journal of Rock Mechanics and Mining Sciences, 107*, 94-109. https://doi.org/10.1016/j.ijrmms.2018.03.008

Tang, Y., Ranjith, P. G., & Wu, B. (2019). Experimental study of effects of shearing on proppant embedment behaviour of tight gas sandstone reservoirs. *Journal of Petroleum Science and Engineering, 172*, 228-246. https://doi.org/10.1016/j.petrol.2018.07.066

Tse, R., & Cruden, D. M. (1979). Estimating joint roughness coefficients. *International Journal of Rock Mechanics and Mining Sciences & Geomechanics Abstracts, 16*(5), 303-307. https://doi.org/https://doi.org/10.1016/0148-9062(79)90241-9

Wang, J., Elsworth, D., & Denison, M. K. (2018). Propagation, proppant transport and the evolution of transport properties of hydraulic fractures. *Journal of Fluid Mechanics, 855*, 503-534. https://doi.org/10.1017/jfm.2018.670

Zhang, F., Fang, Y., Elsworth, D., Wang, C., & Yang, X. (2017). Evolution of Friction and Permeability in a Propped Fracture under Shear. *Geofluids, 2017*, 1-13. https://doi.org/10.1155/2017/2063747

Zhao, Q., Tisato, N., Kovaleva, O., & Grasselli, G. (2018). Direct Observation of Faulting by Means of Rotary Shear Tests Under X-Ray Micro-Computed Tomography. *Journal of Geophysical Research: Solid Earth, 123*(9), 7389-7403. https://doi.org/10.1029/2017jb015394

Zhao, Y., Zhang, L., Wang, W., Liu, Q., Tang, L., & Cheng, G. (2020). Experimental Study on Shear Behavior and a Revised Shear Strength Model for Infilled Rock Joints. *International Journal of Geomechanics, 20*(9). https://doi.org/10.1061/(asce)gm.1943-5622.0001781

Zimmermann, G., & Reinicke, A. (2010). Hydraulic stimulation of a deep sandstone reservoir to develop an Enhanced Geothermal System: Laboratory and field experiments. *Geothermics, 39*(1), 70-77. https://doi.org/10.1016/j.geothermics.2009.12.003

Zoback, M. D., Kohli, A., Das, I., & McClure, M. (2012). *The Importance of Slow Slip on Faults During Hydraulic Fracturing Stimulation of Shale Gas Reservoirs* SPE Americas Unconventional Resources Conference, OnePetro.

550 **Table 1.** Peak shear strengths recovered from the shear tests.

Proppant size (mm)	Normal Stress (MPa)	Peak shear stress (MPa)
No Proppant	2	3.92
No Proppant	3	5.49
No Proppant	4	7.41
No Proppant	5	7.96
0.1-0.5	2	1.83
0.1-0.5	3	3.77
0.1-0.5	4	3.85
0.1-0.5	5	6.37
0.5-1.0	2	1.31
0.5-1.0	3	3.37
0.5-1.0	4	4.28
0.5-1.0	5	5.14
1.0-2.0	2	1.56
1.0-2.0	3	2.56
1.0-2.0	4	3.05
1.0-2.0	5	4.87

551
552

553 **Table 2.** Surface roughness statistics measured both pre- and post-tests.

Proppant size (mm)	Normal Stress (MPa)	Sample No.		Before			After		
				H (mm)	Z_2	RMS	H (mm)	Z_2	RMS
No proppant	2	1-1	Upper	23.22	0.62	3.93	23.52	0.60	3.93
			Lower	41.49	1.17	4.08	22.71	0.61	3.71
No proppant	3	1-2	Upper	18.18	0.55	1.23	5.63	0.23	0.82
			Lower	5.82	0.21	0.85	5.64	0.24	0.83
No proppant	4	1-3	Upper	18.24	0.49	1.35	8.64	0.24	1.52
			Lower	21.96	0.33	1.27	8.53	0.25	1.50
No proppant	5	1-4	Upper	12.92	0.25	2.39	12.27	0.27	2.29
			Lower	13.29	0.25	2.26	12.59	0.27	2.30
0.1-0.5	2	2-1	Upper	6.09	0.17	0.97	5.98	0.16	0.93
			Lower	5.73	0.17	0.96	5.71	0.17	0.91
0.1-0.5	3	2-2	Upper	15.09	0.23	1.83	10.22	0.28	1.83
			Lower	10.77	0.24	1.91	10.32	0.25	1.81
0.1-0.5	4	2-3	Upper	13.65	0.55	1.84	10.10	0.52	1.78
			Lower	10.12	0.47	1.77	10.17	0.53	1.78
0.1-0.5	5	2-4	Upper	8.23	0.24	1.44	8.62	0.27	1.41
			Lower	8.66	0.25	1.38	8.60	0.28	1.38
0.5-1.0	2	3-1	Upper	12.01	0.44	1.52	12.12	0.45	1.54
			Lower	10.08	0.40	1.42	10.32	0.45	1.45
0.5-1.0	3	3-2	Upper	6.78	0.24	1.16	6.66	0.25	1.12
			Lower	7.07	0.23	1.15	6.81	0.24	1.08
0.5-1.0	4	3-3	Upper	18.79	0.52	3.05	18.87	0.51	3.02
			Lower	19.58	0.56	3.13	19.55	0.55	3.17
0.5-1.0	5	3-4	Upper	6.05	0.23	0.77	5.56	0.27	0.81
			Lower	5.97	0.25	0.83	5.61	0.26	0.83
1.0-2.0	2	4-1	Upper	16.08	0.52	2.56	16.62	0.53	2.57
			Lower	16.96	0.52	2.48	17.53	0.54	2.49
1.0-2.0	3	4-2	Upper	14.23	0.55	2.33	14.26	0.54	2.31
			Lower	14.19	0.47	2.29	14.21	0.53	2.30
1.0-2.0	4	4-3	Upper	18.30	0.53	3.13	19.32	0.60	3.39
			Lower	20.25	0.53	3.44	19.14	0.78	3.26
1.0-2.0	5	4-4	Upper	22.99	0.47	1.28	6.62	0.28	1.22
			Lower	8.18	0.26	1.25	7.62	0.29	1.27

554
555

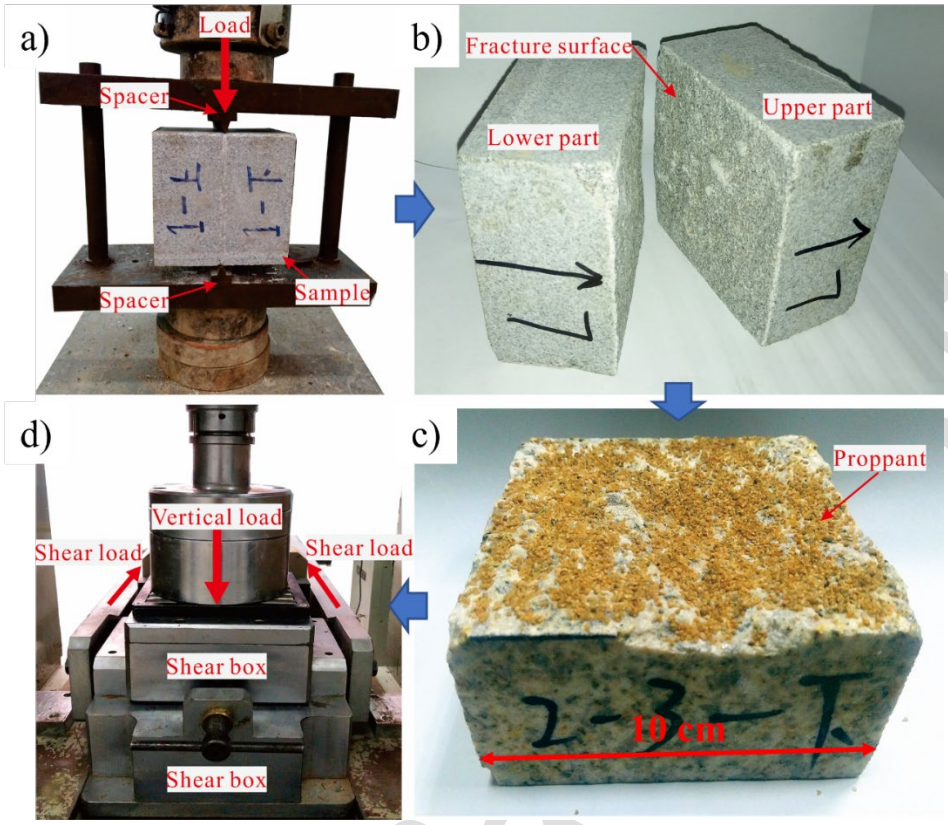

Figure 1. Preparation process for the rough granite fractures used in the direct shear tests. (a & b) Indirect tensile fracture loading to create a fresh rough fracture with matching surfaces. (c) Silica sand proppant placement on the fracture surface using dry pluviation. (d) Test setup of the direct shear test.

563

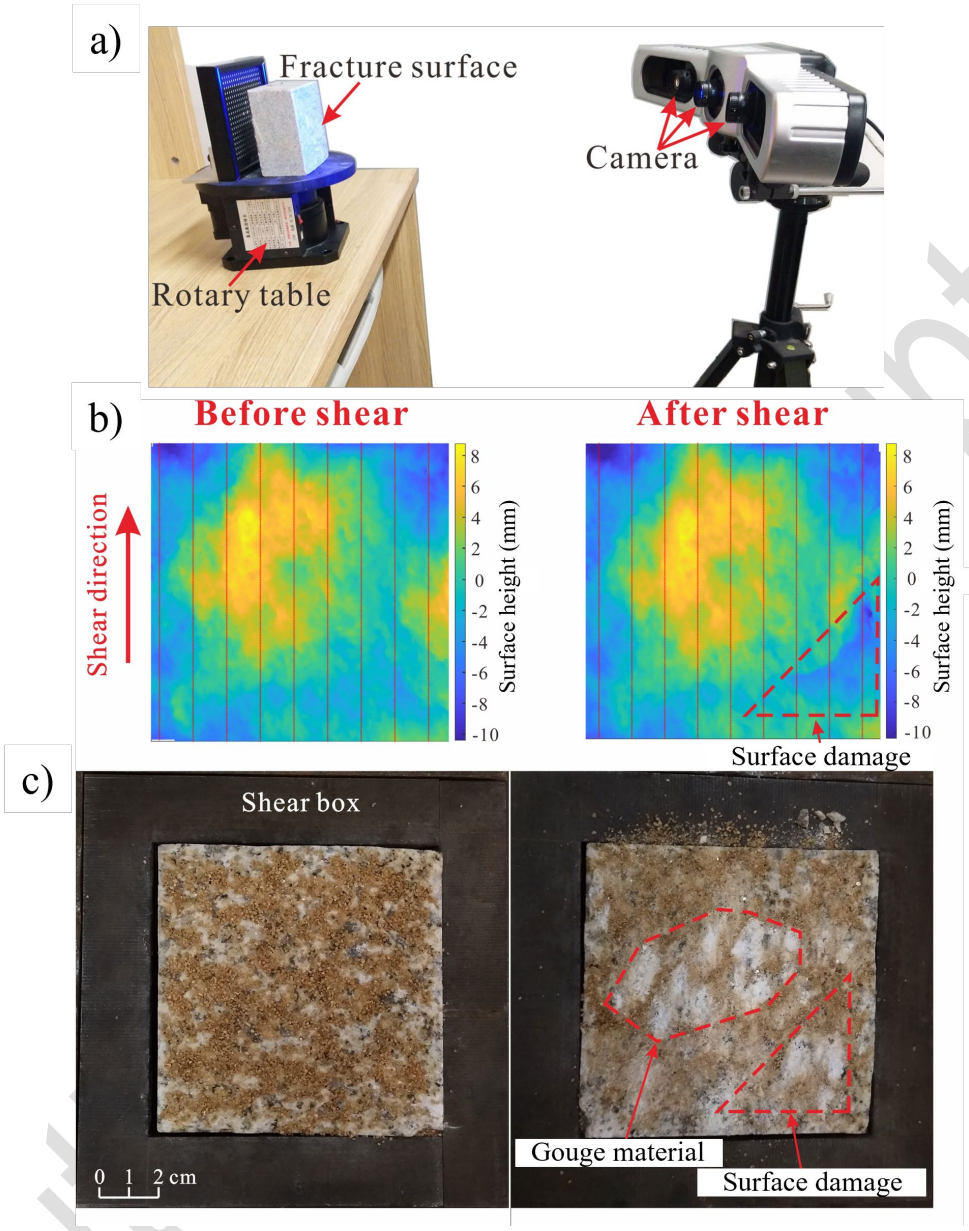

564

565 **Figure 2.** Fracture surface roughness measurement and calculations. (a) Surface scan setup. The
566 surface was digitized into a point cloud with 30 μm spatial resolution. (b) Example results of the
567 surface scan showing the morphological information pre- then post-test (post-test scan was
568 conducted after removing the gouge). The averaged surface roughness was calculated based on
569 nine profiles measured along the shear direction. (c) Example of actual surfaces pre- and then post-
570 test, corresponding to (b).

571

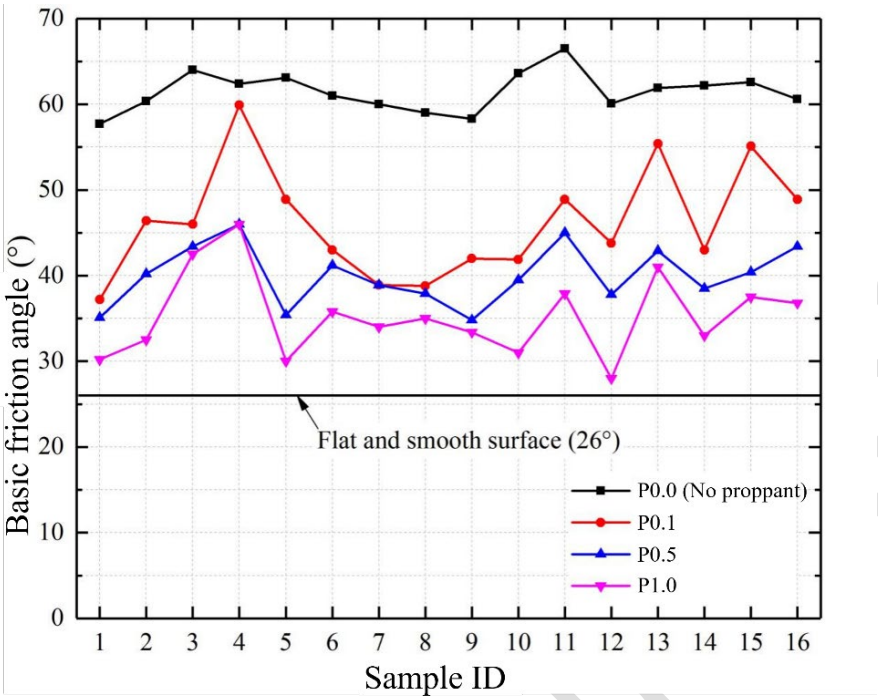

572

573 **Figure 3.** Tilt tests results on rough fractures with four proppant conditions (P0.0, P0.1, P0.5, and
574 P1.0) as well as on a planar, smooth, and pristine fracture to measure the basic friction angle (ϕ_b).

575

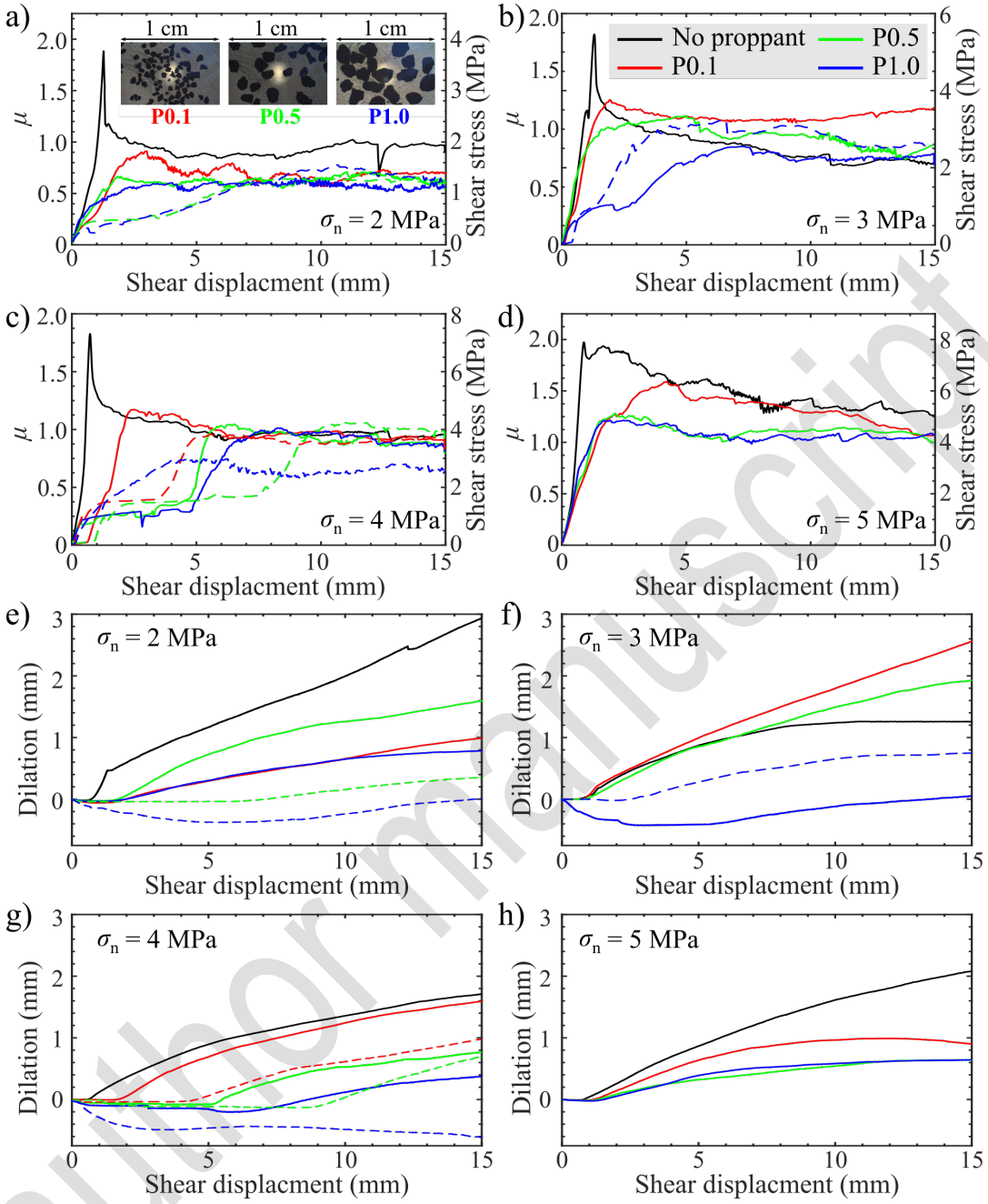

Figure 4. Apparent friction coefficient (a-d) and dilation (e-h) as functions of shear displacement of the fractures under different normal stress and proppant conditions. Solid lines and dashed lines are from the first and second suites of repeated experiments, respectively. Inserts in (a) show the example proppant grains under the microscope. PX.X mnemonics indicate the grain size of the proppant in mm.

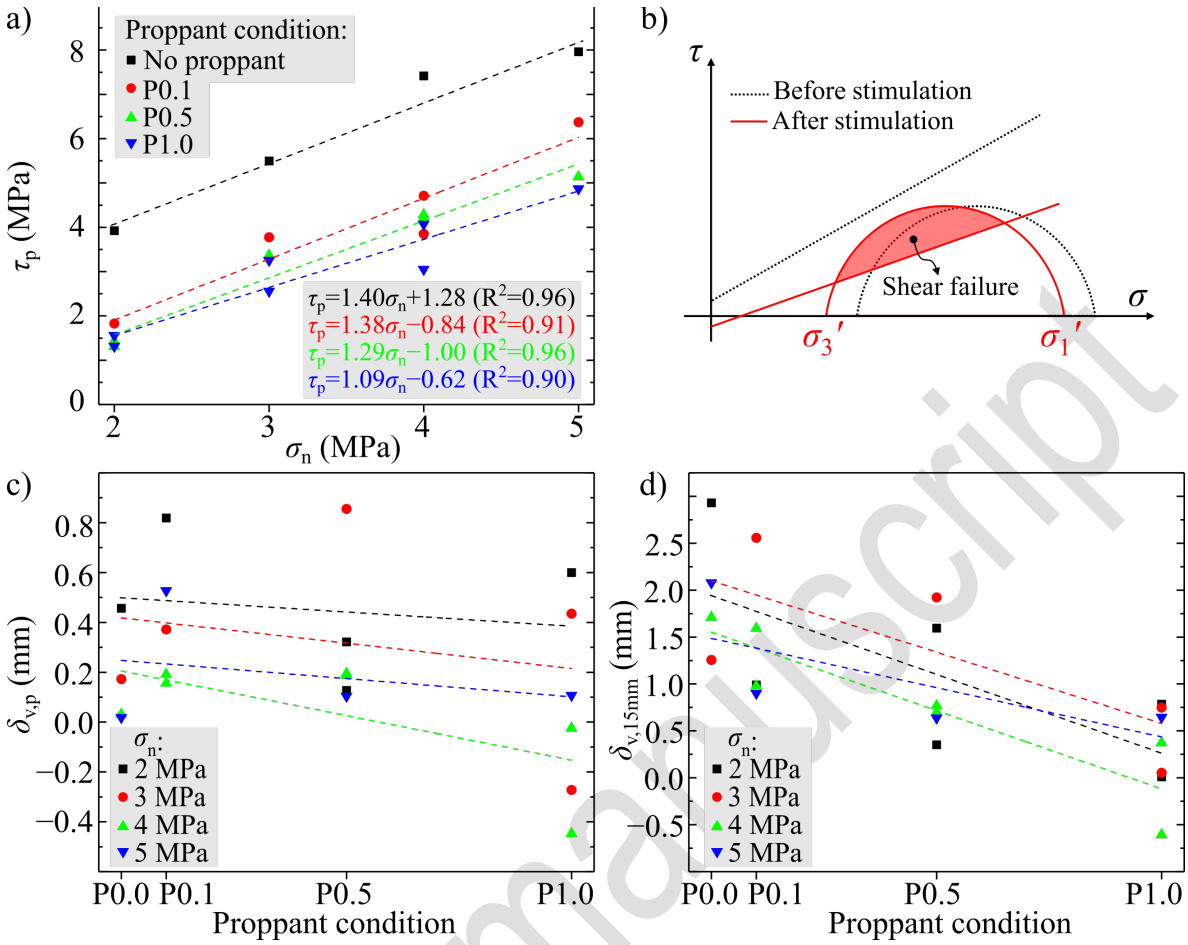

583

584 **Figure 5.** Summary of shear behavior for different normal stress and proppant conditions. (a) Peak
585 shear stress (τ_p) as a function of normal stress (σ_n). (b) Schematic of failure envelope relative to
586 effective principal stresses (σ_1' and σ_3'). (c) Dilation at peak shear stress. (d) Dilation at 15 mm of
587 shear displacement. Dashed lines are linear regressions.

588

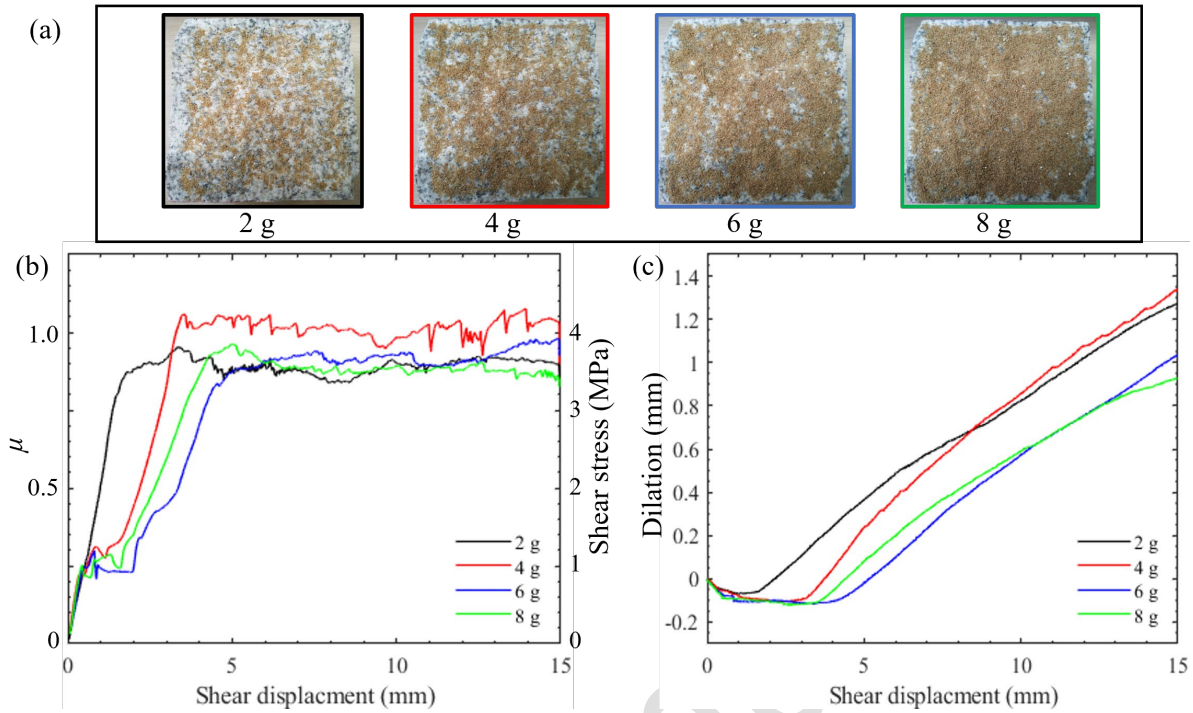

589

590 **Figure 6.** Results of the direct shear experiments conducted under 4 MPa normal stress and with
591 different mass loadings of P0.1 proppant. (a) Illustration of different mass loadings of proppant at
592 2, 4, 6 and 8 grams mass loading per fracture. (b & c) Shear stress and dilation curves.

593

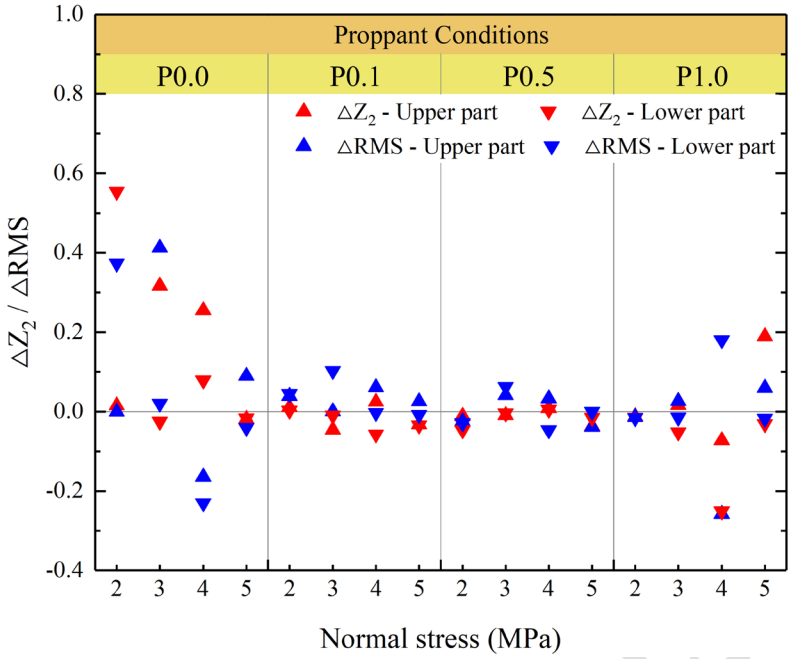

Figure 7. Change in fracture surface roughness (ΔZ_2 and ΔRMS) from pre- to post- experiments and for different normal stress and proppant conditions.

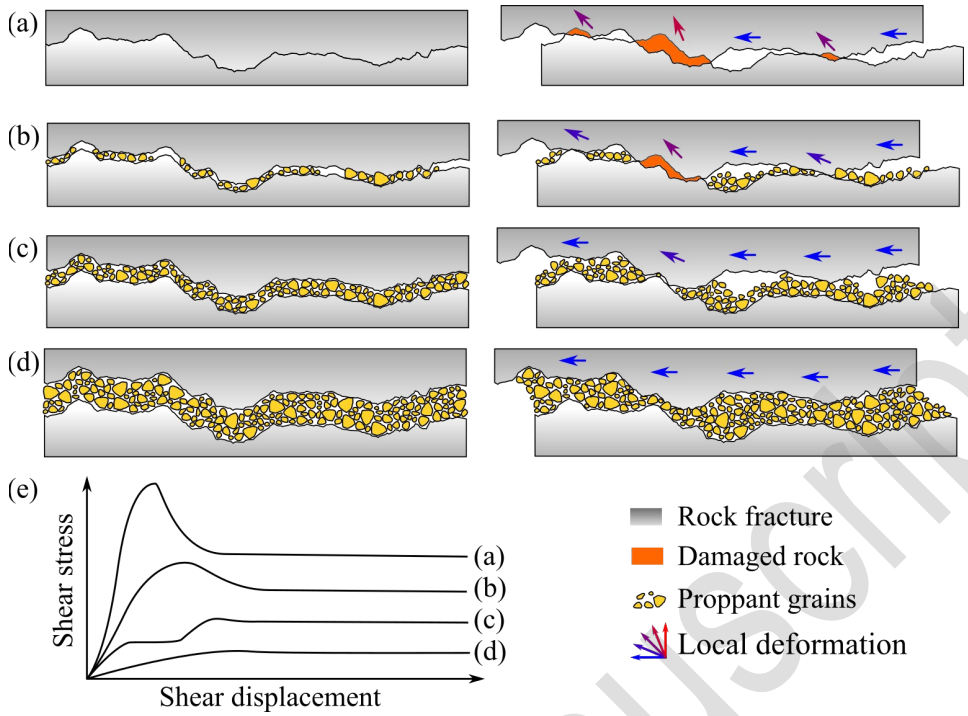

598

599 **Figure 8.** Schematic of mechanisms describing the transition of fracture shear behavior from
600 fracture roughness control (a) to proppant control (d) with increasing mass loading of the proppant.
601 (a-d) Mechanistic illustration of shear behavior with increasing proppant mass loading. (e)
602 Representative τ-δ_s curves corresponding to (a-d).